

A neutron diffraction investigation of high valent doped barium ferrite with wideband tunable microwave absorption

Jun LI^{a,b,*},†, Yang HONG^{c,†}, San HE^{a,b}, Weike LI^{a,b}, Han BAI^{a,b},
Yuanhua XIA^d, Guangai SUN^d, Zhongxiang ZHOU^{a,b,*}

^aSchool of Physics, Harbin Institute of Technology, Harbin 150001, China

^bHeilongjiang Provincial Key Laboratory of Plasma Physics and Application Technology,
Harbin Institute of Technology, Harbin 150001, China

^cSchool of Chemistry and Chemical Engineering, Harbin Institute of Technology, Harbin 150001, China

^dKey Laboratory for Neutron Physics of CAEP, Institute of Nuclear Physics and Chemistry, Mianyang 621999, China

Received: January 30, 2021; Revised: August 20, 2021; Accepted: August 21, 2021

© The Author(s) 2021.

Abstract: The barium ferrite $\text{BaTi}_x\text{Fe}_{12-x}\text{O}_{19}$ ($x = 0.2, 0.4, 0.6, 0.8$) (BFTO- x) ceramics doped by Ti^{4+} were synthesized by a modified sol–gel method. The crystal structure and magnetic structure of the samples were determined by neutron diffraction, and confirm that the BFTO- x ceramics were high quality single phase with sheet microstructure. With x increasing from 0.2 to 0.8, the saturation magnetization (M_s) decreases gradually but the change trend of coercivity (H_c) is complex under the synergy of the changed grain size and the magnetic crystal anisotropy field. Relying on the high valence of Ti^{4+} , double resonance peaks are obtained in the curves of the imaginary part of magnetic conductivity (μ'') and the resonance peaks could move toward the low frequency with the increase of x , which facilitate the samples perform an excellent wideband modulation microwave absorption property. In the $x = 0.2$ sample, the maximum reflection loss (RL) can reach -44.9 dB at the thickness of only 1.8 mm, and the bandwidth could reach 5.28 GHz at 2 mm when RL is less than -10 dB. All the BFTO- x ceramics show excellent frequency modulation ability varying from 18 ($x = 0.8$) to 4 GHz ($x = 0.4$), which covers 81% of the investigated frequency in microwave absorption field. This work not only implements the tunable of electromagnetic parameters but also broadens the application of high-performance microwave absorption devices.

Keywords: barium ferrite; neutron diffraction; microwave absorption

1 Introduction

The rapid development of electronic information

technology and communication industry has increased the requirements of microwave absorption materials to solve the uncovering electromagnetic interference problems [1–3]. Thus, developing microwave absorption materials of large reflection loss (RL) and broad bandwidth are becoming urgent. The inherent properties of microwave absorbing materials, including complex permeability and permittivity, are significant in enhancing

† Jun Li and Yang Hong contributed equally to this work.

* Corresponding authors.

E-mail: J. Li, lijuna@hit.edu.cn;

Z. Zhou, zhouzx@hit.edu.cn

RL and broadening the effective bandwidth [4–6].

The microwave absorption materials can be classified into a resistive type, a dielectric type, and a magnetic medium type according to the loss mechanism [7–9]. The resistive absorbing materials mainly absorb electromagnetic wave by interaction with an electric field, and the absorption efficiency depends on the conductivity and dielectric constant, include carbon black, metal powder, silicon carbide, graphite, and special carbon fiber [10]. For dielectric absorbing materials, the electromagnetic wave is mainly absorbed by the dielectric polarization relaxation loss, and the typical representative is barium titanate ferroelectric ceramics [11]. The attenuation of the electromagnetic wave by the magnetic medium type absorbing materials mainly comes from resonance and hysteresis loss, such as ferrite and carbonyl iron [12,13]. Among all these materials, the ferrite is an ideal microwave absorbing material for the simple preparation process and the stable performance [14–16].

M-type barium ferrite ($\text{BaFe}_{12}\text{O}_{19}$, abbreviated as BaM), a versatile material, performs excellent electromagnetic properties due to the large magnetic loss at the natural resonance frequency. Pure barium ferrite has large saturation magnetization (M_s), high coercivity, magnetic anisotropy constants, and the large magnetic loss at the natural resonance frequency, which make barium ferrite have excellent microwave absorption characteristics [17,18]. To investigate larger RL, broader bandwidth, and even tunable microwave absorbing material, many kinds of research work on barium ferrite doping modification are carried out [19,20]. The magnetic loss is related to the content of Fe^{3+} in barium ferrite, and thus the microwave absorption properties can be adjusted when Fe^{3+} ions are substituted with other trivalent ions or combination of divalent and tetravalent ions [21]. BaM-based cationic substitutions for Fe^{3+} are used to modify the dielectric and magnetic parameters, which play an important role in RL calculation. The substitutions for Fe^{3+} of BaM-based can be divided into two main approaches: covalent cation substitution, such as Ga^{3+} , In^{3+} ; and Er^{3+} and heterovalent cationic combination, such as $\text{Co}^{2+}-\text{Ti}^{4+}$, $\text{Co}^{2+}-\text{Zr}^{4+}$, and $\text{Ni}^{2+}-\text{Ti}^{4+}$ [22–26]. However, recent studies have shown that the introduction of high-valence ions destroys the valence state equilibrium of barium ferrite, resulting in multiple absorption peaks, which can increase the bandwidth of electromagnetic wave absorption of the material [27–29].

In this work, we synthesized $\text{BaFe}_{12-x}\text{Ti}_x\text{O}_{19}$ (BFTO- x , $x = 0.2, 0.4, 0.6, 0.8$) using only tetravalent Ti^{4+} ions as high valent dopant ions by a modified sol–gel method. We systematically analyzed the structure, morphology, magnetic properties, and electromagnetic parameters of the sample. By comparing the magnetic structure of the neutron diffraction with the experimental magnetic results, the internal magnetic mechanism of the sample was deeply studied. The modified M-type barium ferrite exhibits better tunability for electromagnetic properties, which has a positive role on the exploration of the novel microwave absorbing materials.

2 Experimental

2.1 Material synthesis

The Ti^{4+} doped M-type barium ferrite ceramics ($\text{BaFe}_{12-x}\text{Ti}_x\text{O}_{19}$, $x = 0.2, 0.4, 0.6, 0.8$) were prepared utilizing the modified sol–gel method that is more effective than conventional solid state method. Barium nitrate ($\text{Ba}(\text{NO}_3)_2$), iron nitrate ($\text{Fe}(\text{NO}_3)_3 \cdot 9\text{H}_2\text{O}$), and titanium nitrate ($\text{Ti}(\text{NO}_3)_4$) were weighted in a stoichiometric ratio and dissolved in citric acid solution adequately. The pH value of the solution was adjusted to 8 by adding ammonia water, and then the solution was stirred for 2 h and aged for 12 h at room temperature. The mixed solution was placed in 80 °C water bath for 3 h to form a sol, which was then transferred to a dry box at 120 °C for 1–2 days until a dry gel was formed. The aerogel was incubated at 210 °C for 3 h to remove organic components from the gel. Calcination was carried out at 1200 °C to get the BFTO- x powder. The powder mixed with polyvinyl alcohol (PVA) was pressed into wafers of 13 mm in diameter and sintered at 600 °C for 4 h to eliminate the binder, and then the wafers were sintered at 1200 °C for 4 h in air atmosphere to obtain the BFTO- x ceramics.

2.2 Characterizations

The neutron powder diffraction (NPD) experiments were carried out at room temperature using the high resolution neutron powder diffractometer (HRND) ($\lambda = 1.884 \text{ \AA}$) at China Mianyang Research Reactor (CMRR), and the corresponding Rietveld refinement was achieved by FullProf and the simulated annealing and representational analysis (SARAh). Morphologies were examined using the field emission scanning electron microscopy (SEM; ZEISS Merlin Compact).

Magnetic properties were investigated using a vibrating sample magnetometer (VSM, Lake Shore 7404). The electromagnetic properties were studied using the air-line method, which were mixed with PVA at a mass ratio of 6:1. The complex permittivity and permeability were measured through the coaxial method from 2 to 18 GHz on a vector network analyzer (Keysight Technologies N5234A), and the sample and paraffin were mixed at a mass ratio of 7:3 and then compressed into a test ring with an outer diameter of 7 mm and an inner diameter of 3 mm.

3 Results and discussion

3.1 Effects of titanium substitution on crystal structure and microstructure

The neutron diffraction patterns of BFTO-*x* (*x* = 0.2, 0.4, 0.6, 0.8) ceramics are shown in Fig. 1(a), which contains the complete neutron diffraction pattern before and after refinement using Rietveld method. Since the neutron diffraction patterns include both structural and magnetic information, the process of BFTO-*x* refinement using FullProf can be divided into two parts: structural and magnetic phases [30]. The detailed results of refinement contained structural and magnetic parameters also appear in Fig. 1(a), and the corresponding refinement factors of each components are also shown in Fig. 1(a). Compared with the neutron diffraction Bragg positions of pure barium ferrite, no other impurity peaks were found, indicating that the four components were single phase with space

group *P63/mmc*. Moreover, the corresponding magnetic space group of BFTO-*x* is *R-3m:H*, which was determined by utilizing the SARA_H Analysis to calculate the possible magnetic space groups [31]. The result of structural refinement shows that the lattice parameters change little with the increasing of Ti doping, and the corresponding parameters are *x* = 0.2 (*a* = *b* = 5.8946 Å, *c* = 23.2225 Å), *x* = 0.4 (*a* = *b* = 5.8940 Å, *c* = 23.2354 Å), *x* = 0.6 (*a* = *b* = 5.8942533 Å, *c* = 23.2402 Å), and *x* = 0.8 (*a* = *b* = 5.8944 Å, *c* = 23.2361 Å). The change may origin from that Ti ion occupies the position of Fe ion in the sublattice, and the atomic radius of Ti⁴⁺ ion (0.0605 nm) is basically the same with that of Fe³⁺ ion (0.0645 nm). The distortion of lattice structure stems from the replacement of Ti ions, leading to the concomitant changed of cell parameters. Another parameter characterizing the crystal and magnetic structure is the Bragg position. The structure of Bragg position has not changed with the Ti doping, which is corresponded with the refinement result of lattice parameters. However, the magnetic Bragg position changes with the increase of Ti doping. With the increase of Ti, in order to keep the valence conserve, part of Fe³⁺ ions converted into Fe²⁺ ions, generating new Holland factor. Therefore, new Bragg position generated when *x* = 0.6. In addition, more analyses about structure are shown in Fig. S1 in the Electronic Supplementary Material (ESM).

Figure 1(b) shows that the primitive cell of BaFe₁₂O₁₉ is composed of 10 O²⁻ ion layers, because the radii of Ba²⁺ ion (0.142 nm) and O²⁻ ion (0.140 nm) are not much different, and Ba²⁺ ion often occupies the

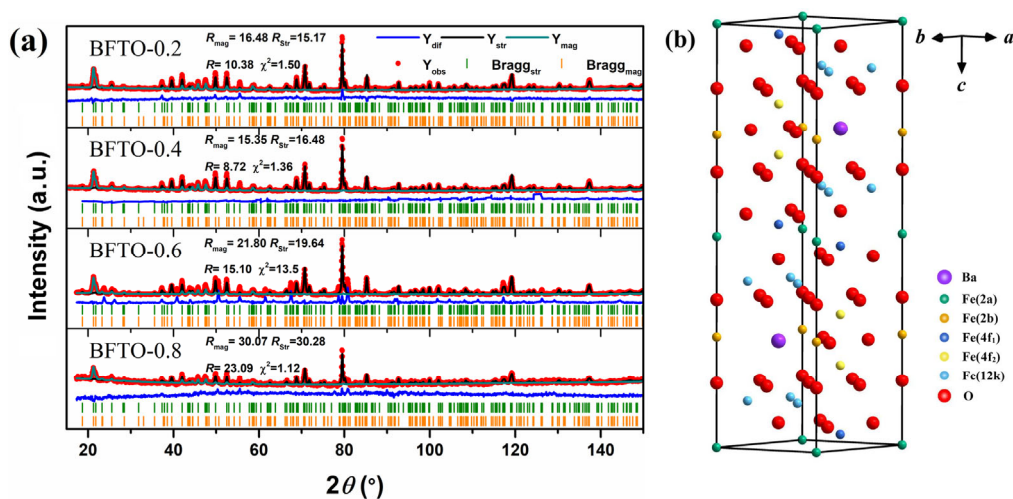


Fig. 1 (a) Neutron diffraction and corresponding refinement patterns of BFTO-*x* (*x* = 0.2, 0.4, 0.6, 0.8) ceramics and (b) schematic structure of BaFe₁₂O₁₉.

position of O^{2-} ion in the oxygen lattice of the crystal. Therefore, certain amounts of barium ions are contained in the close-packed structure of oxygen ions. Meanwhile, Fe^{3+} ions exist in the interstices of oxygen ions, forming a stable hexahedral structure. Fe^{3+} ions are distributed over five different positions in $BaFe_{12}O_{19}$, named 12k, 2a, 2b, $4f_1$, and $4f_2$ [32]. Magnetic moment orientations of Fe^{3+} in three positions (12k, 2a, 2b) spin up while those of $4f_1$ and $4f_2$ positions spin down. In order to obtain the information of exact occupation of Ti, the method of neutron diffraction intensity fitting was utilized to explore the occupation probability of Ti as listed in Table 1. The result of fitting shows that Ti tends to occupy the position 2a, 2b, and 12k, in where Fe is spin-up.

The surface morphologies of BFTO- x ceramics are shown in Fig. 2. It can be observed that all components

Table 1 Occupation probability of BFTO- x ceramics

	$x = 0.2$	$x = 0.4$	$x = 0.6$	$x = 0.8$
2a(Fe)	0.08292	0.08290	0.08083	0.07965
2a(Ti)	0.00041	0.00043	0.00250	0.00368
2b(Fe)	0.07125	0.05427	0.04083	0.02923
2b(Ti)	0.01208	0.02906	0.04250	0.05410
12k(Fe)	0.49582	0.49830	0.49500	0.49114
12k(Ti)	0.00417	0.00170	0.00500	0.00860

perform typical hexagonal plates, and the grain boundary is distinct. The particle size of BFTO- x ceramics varies with the increase of x , where the grain size of BFTO-0.4 about $1 \mu m$ is larger than those of the other three components. Compared with the solid state sintering method, the grain size of BFTO ceramics prepared by the sol-gel process is smaller, which has an important effect on coercive force [33].

3.2 Effects of titanium substitution on magnetic properties

The magnetic properties of BFTO- x ($x = 0.2, 0.4, 0.6, 0.8$) ceramics are derived from magnetic hysteresis loops at room temperature in Fig. 3. It can be seen that all samples are approaching saturation as the applied field is increased up to 15 kOe. With x increasing from 0.2 to 0.8, the M_s decreases gradually from 31.87 to 22.13 emu/g, while the change trend of coercivity (H_c) is complicated. The change trend of M_s and H_c is related to the magnetic moment of Fe^{3+} and the occupied position during doping [34,35].

The replacement from Ti^{4+} ion to the magnetic Fe^{3+} ion ($5 \mu B$) would reduce the M_s of barium ferrite ceramics since the Ti^{4+} ion is non-magnetic, and M_s exhibits a downward trend with the increase of Ti^{4+} ion doping due to the decrease of super-exchange effect

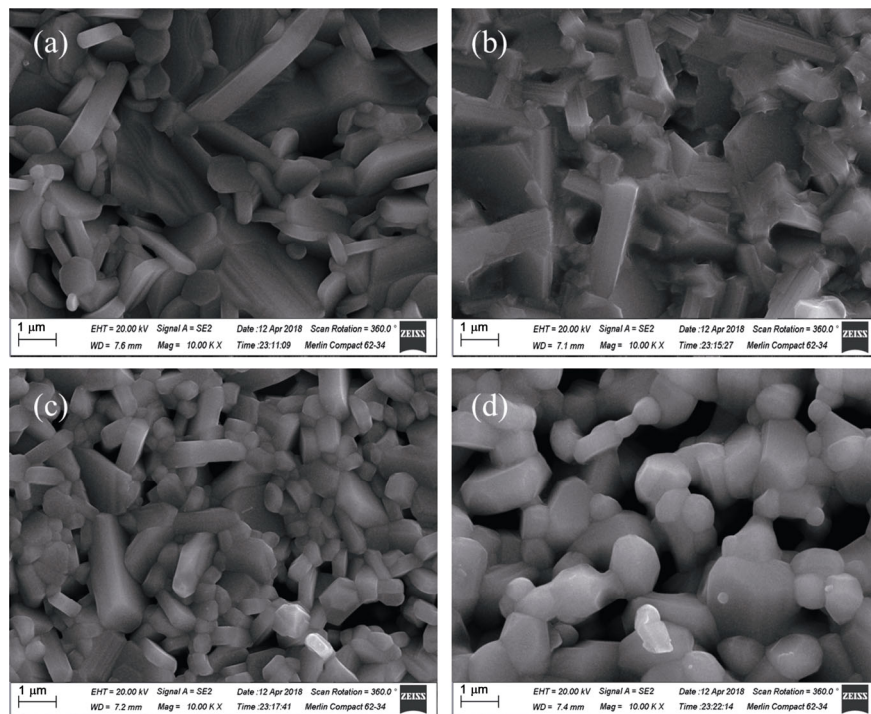


Fig. 2 SEM images of BFTO- x ceramics with (a) $x = 0.2$, (b) $x = 0.4$, (c) $x = 0.6$, and (d) $x = 0.8$.

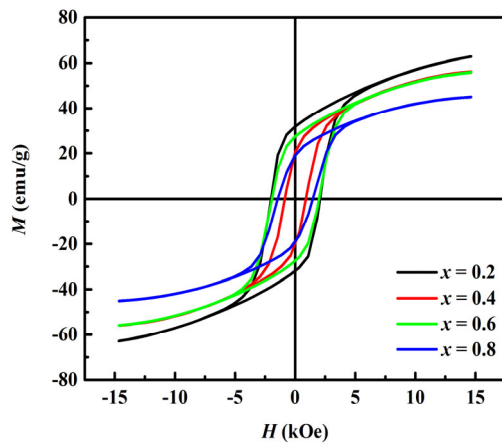


Fig. 3 Magnetic hysteresis loops ($M-H$) of samples at room temperature.

between $Fe^{3+}-O_2-Fe^{3+}$ [36]. It is known that H_c is mainly affected by anisotropic field (H_a) and grain size [37,38]. That is, the larger the grain size of ceramics, the smaller the H_c . On the other hand, H_c is proportional to H_a . According to the formula $H_a = 2K_1/M_s$, H_a is proportional to the magnetic crystal anisotropy constant (K_1), and inversely proportional to M_s [39,40]. According to the contribution of different lattice positions to K_1 , the 2b position has the greatest effect on K_1 . Therefore, the more components are doped, the greater the effect on H_c . For the components $x = 0.2, 0.6,$ and 0.8 , H_c has a declining trend with the increase of the doping. Because the changes of the grain size and M_s are weak, the declining trend of the H_c is contributed to the influence of K_1 . The reason for the sharp decline of H_c of BFTO-0.4 ceramic sample is relatively complex and can be attributed to two aspects [41,42]. Firstly, the SEM image of BFTO- x ceramics shows that the grain size of BFTO-0.4 ceramic sample is larger than that of other components, so the H_c of BFTO-0.4 ceramic will be smaller. Secondly, the increase of Ti^{4+} doping and the occupied position would have a greater influence on K_1 , which also causes the obvious change of H_c . However, compared to BFTO-0.2 ceramic sample, the M_s change of BFTO-0.4 ceramic sample is smaller than that of BFTO-0.2. Therefore, the effect of M_s on H_c can be neglected, and the change of H_c mainly depends on the grain size and K_1 .

Moreover, refined magnetic structure shows that non-collinear magnetic structure exists in BFTO- x ceramics [30,43]. The magnetic moment of primitive cell varies with the doping content of Ti, which is the same with experimental data, and the corresponding results are listed in Table 2. The experimental magnetic

Table 2 Magnetic moment of BFTO- x ceramics' primitive cell

	$x = 0.2$	$x = 0.4$	$x = 0.6$	$x = 0.8$
Experimental (μB)	12.056	11.138	10.819	11.731
Theoretical (μB)	17.167	14.421	11.907	14.231

moment of primitive cell (M_{pc}) was calculated by Eq. (1):

$$M_{pc} (\mu B) = \frac{M_s (\text{emu/g}) \times 1.0783 \times 10^{20}}{N_A} \times M(\text{BFTO-}x) \quad (1)$$

where $M(\text{BFTO-}x)$ is the molar mass of BFTO- x and N_A is the Avogadro constant. From the result of magnetic refinement, the theoretical M_{pc} fluctuates with the increase of Ti doping, which is consistent with the trend of experimental result.

3.3 Effects of titanium substitution on electro-magnetic and microwave absorption properties

The complex permittivity ($\epsilon = \epsilon' - j\epsilon''$) and complex permeability ($\mu = \mu' - j\mu''$) of BFTO- x ceramics are shown in Fig. 4, which are measured by the air-line method within 2–18 GHz. As observed, the real part of permittivity ϵ' of $x = 0.4$ component can reach 25, while the ϵ' of the other components is smaller to some extent. For the imaginary part of permittivity ϵ'' , there are remarkable dielectric relaxation phenomena in all samples, which can contribute to increasing RL of the absorbing sample. In Fig. 4(d), the apparent resonance phenomenon can be observed. It is necessary to note that the natural resonance frequency of the component $x = 0.2$ is larger than 18 GHz, while the natural resonance frequency of the other three components at a frequency range of 6–14 GHz illustrated in the inset of Fig. 4(d) is within the measured frequency range.

According to the formula $f_r = 1.4gH_a$, the natural resonant frequency (f_r) is correlated with the magnetic H_a of the ceramic sample and the Holland factor (g) [44]. Due to the low H_a of BFTO-0.4 ceramic, the natural resonant frequency of the $x = 0.4$ sample is the lowest and appears near 8 GHz, while double resonance peaks were obtained in $x = 0.6$ and $x = 0.8$ components. The high-valence ionic Ti^{4+} doping, which destroys the valence equilibrium of barium ferrite, will produce a new g factor, and the appearance of double resonance peaks shows that there are two g factors in these samples. With the increase of Ti^{4+} doping, the H_a decreases, and the natural resonance frequency moves to the lower frequency range. Therefore,

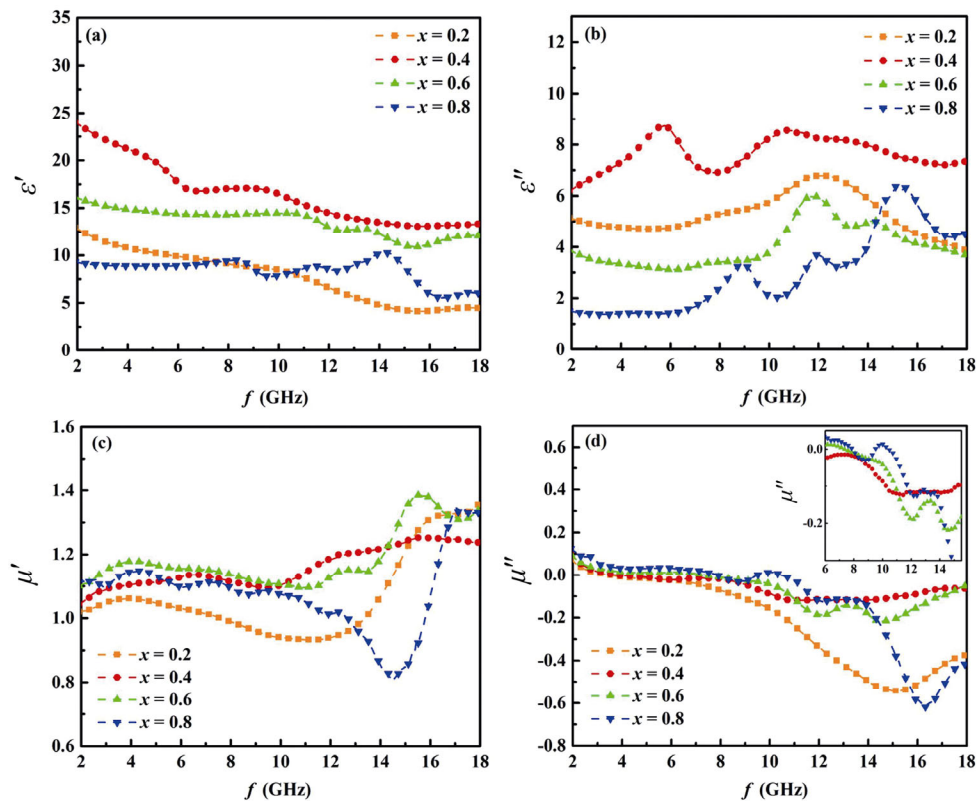


Fig. 4 Electromagnetic parameters of PVA mixed BFTO- x ceramics: (a) real parts and (b) imaginary parts of the complex permittivity, and (c) real parts and (d) imaginary parts of the complex permeability.

the appearance of double resonance peak is advantageous to obtain the larger bandwidth. More evidence can be found in Fig. S2 in the ESM, which shows the dielectric and magnetic loss of PVA mixed BFTO- x ceramics. The large dielectric and magnetic loss was obtained in the $x = 0.2$ sample, which indicates a large RL. The loss curves of $x = 0.6$ and 0.8 have evident fluctuation, and could get large bandwidth.

The RL of PVA mixed BFTO- x ceramics can be calculated from the measured electromagnetic parameters [45], as shown in Fig. 5. Relying on the dielectric and magnetic loss, the four components of PVA mixed BFTO- x ceramics have obtained a large RL. The maximum RL of -44.9 dB means that the absorption of electromagnetic waves can reach 99.99% which was obtained in the $x = 0.2$ sample, and the thickness is relatively thin, only 1.8 mm. The absorption of electromagnetic waves can also reach 90% in the other three components. The apparent double absorption peaks appear in Figs. 5(c) and 5(d), which maybe origin from the presence of more than one of the Holland factors in the wave-absorbing material that

can benefit for widening the bandwidth of the material. RL and bandwidth are two important indexes to evaluate the performance of absorbing materials, and high-loss and large-bandwidth materials can be used in a wider range of applications [46].

Figure 6 shows the 3D RL contour plots of BFTO- x ceramics, and all samples perform wide bandwidth in the specific frequency and thickness. Although the absorption of electromagnetic waves by this material is not the best, we can find that with the doping of Ti^{4+} ions, the absorbing properties of M-type barium ferrite have changed significantly. This change is mainly due to the transition of trivalent Fe ions to divalent Fe ions, which affects the permeability of the material and the impedance matching, and broadens the absorbing effect at high frequencies [47–49].

Figure 7(a) shows the relationship between bandwidth and RL of BFTO- x samples, and the maximum RL and bandwidth are listed in Table 3. For $x = 0.2$, the greatest loss can be obtained at the thickness of 1.8 mm, and the bandwidth can reach 5.28 GHz at 2 mm when RL is less than -10 dB, while the bandwidth of the other three components is about 3 GHz.

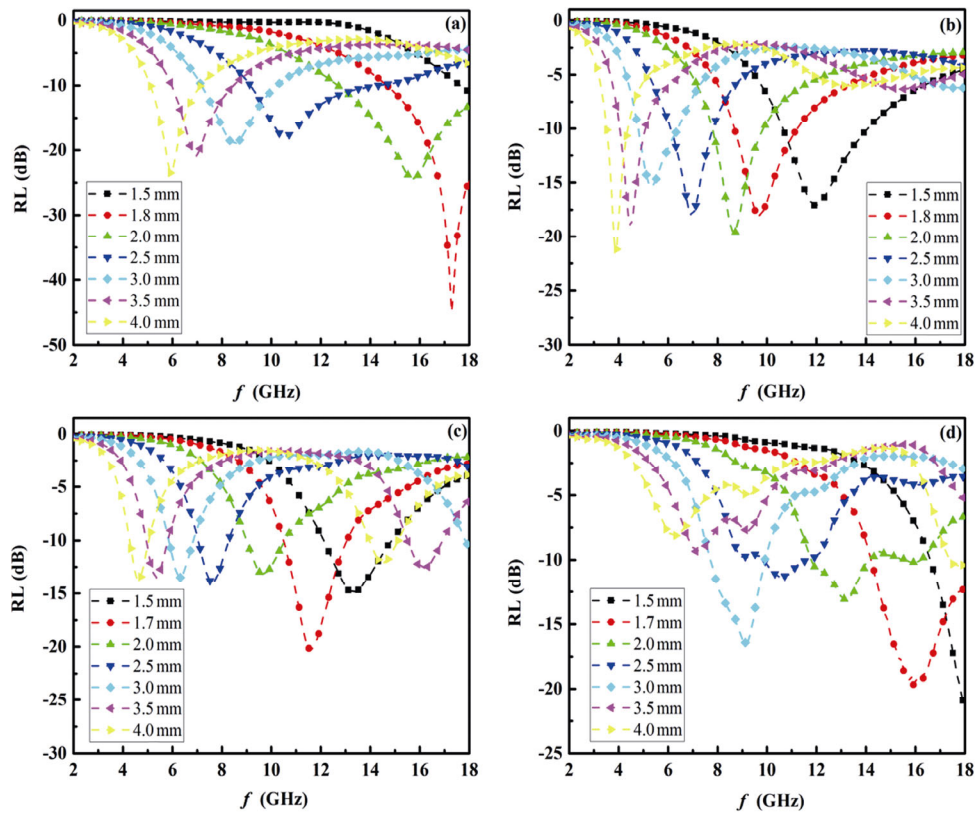


Fig. 5 RL curves of PVA mixed BFTO-*x* ceramics in the frequency range of 2–18 GHz: (a) *x* = 0.2, (b) *x* = 0.4, (c) *x* = 0.6, and (d) *x* = 0.8.

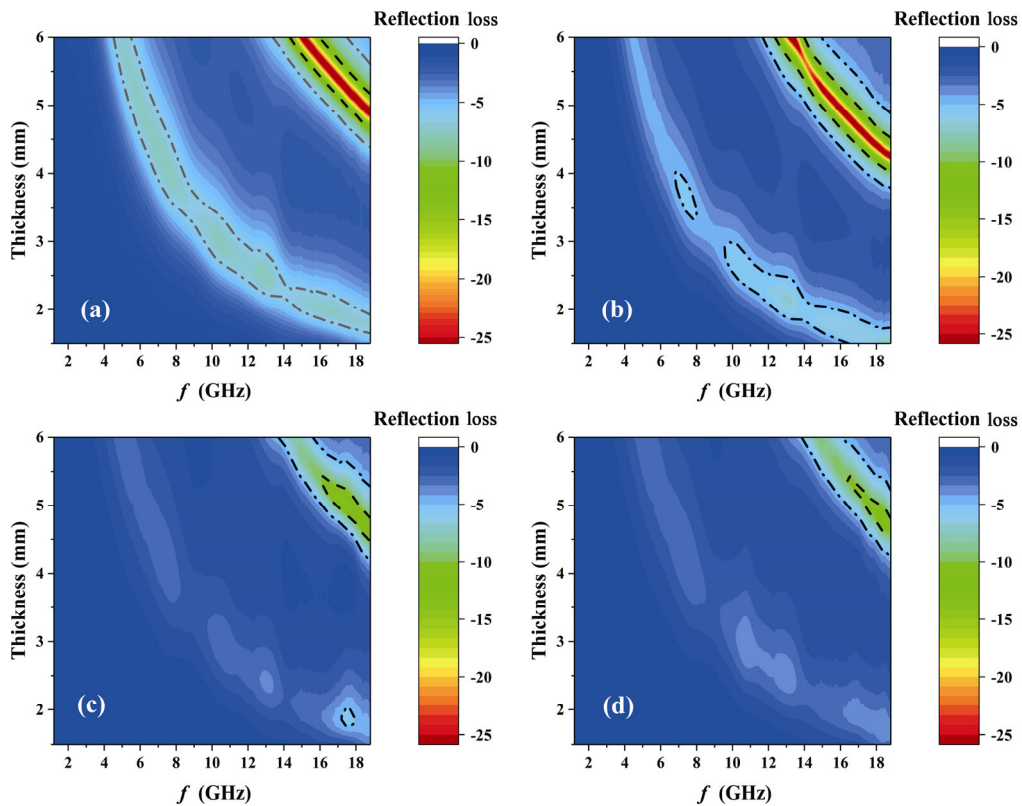


Fig. 6 3D RL contour plots of BFTO-*x* ceramics: (a) *x* = 0.2, (b) *x* = 0.4, (c) *x* = 0.6, and (d) *x* = 0.8.

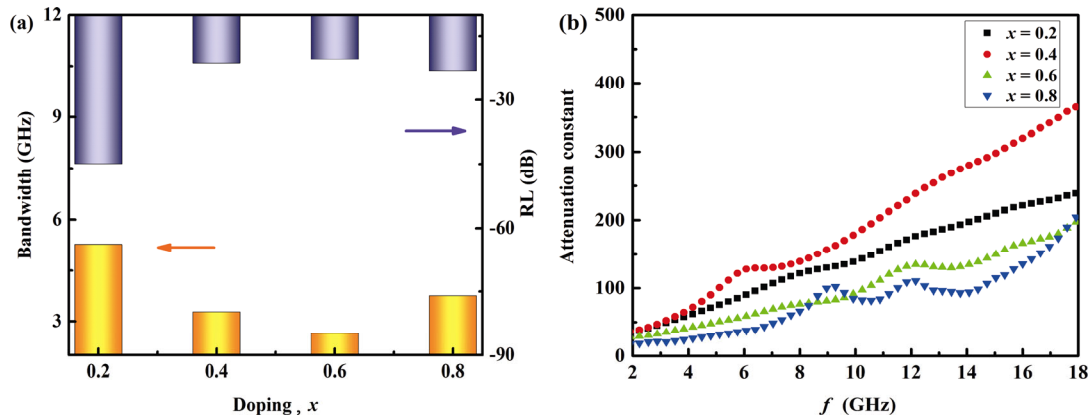


Fig. 7 (a) Maximum RL and the corresponding bandwidth over -10 dB of each component and (b) attenuation constant of BFTO-x ceramics.

Table 3 Maximum RL and corresponding bandwidth over -10 dB of PVA-mixed BFTO-x ceramics

Component	Thickness (mm)	Maximum RL (dB); position (GHz)	Bandwidth <-10 dB (GHz)
x = 0.2	1.8	-44.93; 17.28	3.28
x = 0.4	1.5	-17.1; 11.92	3.28
x = 0.6	1.7	-20.3; 11.6	2.48
x = 0.8	1.7	-19.6; 15.92	3.76

In the ion-doped barium ferrite ceramic, the strong absorbing ability originates from the high attenuation constant [50]. The attenuation constant is expressed by Eq. (2):

$$\alpha = \left(\frac{\sqrt{2\pi f}}{c} \right) \sqrt{(\mu''\epsilon'' - \mu'\epsilon') + \sqrt{(\mu''\epsilon'' - \mu'\epsilon')^2 + (\epsilon''\mu'' + \epsilon''\mu')^2}} \quad (2)$$

where f is the microwave frequency and c is the velocity of light. According to Eq. (2), the attenuation constants of the four components of BFTO-x ceramics can be calculated, as shown in Fig. 7(b). Within the measuring frequency range of 2–18 GHz, four components have a large attenuation constant, wherein the attenuation constant of $x = 0.4$ component is the largest, 350. The variation trend of attenuation constants is similar to that of the imaginary part of magnetic permeability, and there is a double resonance peak in $x = 0.6$ and 0.8 components. Therefore, the dielectric constant and permeability are the two parameters that determine the microwave absorbing performance, and magnetic and dielectric loss is critical to improve the attenuation of materials to electromagnetic waves.

Besides, frequency modulation is also a standard for measuring the overall performance of absorbing

materials. As can be seen from Figs. 4–7, the excellent frequency modulation can be obtained in the four components of BFTO-x ceramics. RL peaks of the $x = 0.2$ component are reduced from ~17 to 6 GHz with varying thicknesses, and the frequency modulation range covers 69% of the measuring frequency range, enabling the control of a wide range of absorption frequencies. The frequency regulation ranges of $x = 0.4$, 0.6, and 0.8 components are 4–12, 5–18, and 6–18 GHz, respectively. Compared with Refs. [5,17,22], both the effective absorption bandwidth and the maximum loss of BFTO ceramics have been enhanced to a certain extent in this work. The maximum RL peaks of the four components also moved with the Ti^{4+} doping content, varying from 18 GHz ($x = 0.8$) to 4 GHz ($x = 0.4$), which covers 81% of the investigated frequency. In conclusion, all of the four components of BFTO-x ceramics show excellent frequency modulation ability.

4 Conclusions

The hexagonal sheet like $BaTi_xFe_{12-x}O_{19}$ ($x = 0.2, 0.4, 0.6, 0.8$) ceramics were synthesized by a modified sol-gel method. Through the refined analysis of neutron diffraction, Ti^{4+} tends to occupy the position 2a, 2b, and 12k of the structure. M_s decreases gradually with the increase of Ti^{4+} doping, but the change of the coercive force is complex under the synergy of the changed grain size and the magnetic crystal anisotropy field. The excellent microwave absorption performance -44.9 dB with board bandwidth in the $x = 0.2$ component can be attributed to the double resonance peak induced by high valent doping of Ti^{4+} . Meanwhile, the RL peak position of the $x = 0.6$ component can be

adjusted from 18 to 5 GHz and the remaining components cover up to 50% of the frequency adjusted range, which have a significant potential application value in microwave absorption field.

Acknowledgements

This work was supported by the National Natural Science Foundation of China (U2130110 and 51502054).

Electronic Supplementary Material

Supplementary material is available in the online version of this article at <https://doi.org/10.1007/s40145-021-0529-3>.

References

- [1] Toneyuzo P, Viau G, Acher O, *et al.* Monodisperse ferromagnetic particles for microwave applications. *Adv Mater* 1998, **10**: 1032–1035.
- [2] Singh C, Kaur H, Bindra Narang S, *et al.* Investigation of microwave absorption and DC electrical properties of Mn²⁺ and Ti⁴⁺ substituted SrMn_xTi_xFe_(12-2x)O₁₉ ferrite. *J Alloys Compd* 2016, **683**: 302–307.
- [3] Joshi R, Singh C, Singh J, *et al.* A study of microwave absorbing properties in Co–Gd doped M-type Ba–Sr hexaferrites prepared using ceramic method. *J Mater Sci: Mater Electron* 2017, **28**: 11969–11978.
- [4] Che R, Peng LM, Duan X, *et al.* Microwave absorption enhancement and complex permittivity and permeability of Fe encapsulated within carbon nanotubes. *Adv Mater* 2004, **16**: 401–405.
- [5] Singh J, Singh C, Kaur D, *et al.* Microwave absorbing characteristics in Co²⁺ and Al³⁺ substituted Ba_{0.5}Sr_{0.5}Co_xAl_xFe_{12-2x}O₁₉ hexagonal ferrite. *J Mater Sci Mater Electron* 2017, **28**: 2377–2384.
- [6] Liu CY, Zhang YT, Zhang YJ, *et al.* Multiple nature resonance behavior of BaFe_xTiO₁₉ controlled by Fe/Ba ratio and its regulation on microwave absorption properties. *J Alloys Compd* 2019, **773**: 730–738.
- [7] Ding Y, Zhang L, Liao QL, *et al.* Electromagnetic wave absorption in reduced graphene oxide functionalized with Fe₃O₄/Fe nanorings. *Nano Res* 2016, **9**: 2018–2025.
- [8] Li J, Xu TT, Liu LL, *et al.* Microstructure, magnetic and low-frequency microwave absorption properties of doped Co–Ti hexagonal barium ferrite nanoparticles. *Ceram Int* 2021, **47**: 19247–19253.
- [9] Ye XL, Chen ZF, Ai SF, *et al.* Porous SiC/melamine-derived carbon foam frameworks with excellent electromagnetic wave absorbing capacity. *J Adv Ceram* 2019, **8**: 479–488.
- [10] Chiu SC, Yu HC, Li YY. High electromagnetic wave absorption performance of silicon carbide nanowires in the gigahertz range. *J Phys Chem C* 2010, **114**: 1947–1952.
- [11] Saini P, Arora M, Gupta G, *et al.* High permittivity polyaniline–barium titanate nanocomposites with excellent electromagnetic interference shielding response. *Nanoscale* 2013, **5**: 4330.
- [12] Jia JG, Liu CY, Ma N, *et al.* Exchange coupling controlled ferrite with dual magnetic resonance and broad frequency bandwidth in microwave absorption. *Sci Technol Adv Mater* 2013, **14**: 045002.
- [13] Liu CY, Fang G, Li Z, *et al.* Achieving impressive millimeter-wave absorption properties in Nb⁵⁺ doped Barium ferrite by simply controlling the sintering atmosphere. *Mater Lett* 2019, **244**: 147–150.
- [14] Pullar RC. Hexagonal ferrites: A review of the synthesis, properties and applications of hexaferrite ceramics. *Prog Mater Sci* 2012, **57**: 1191–1334.
- [15] Kaur R, Dhillon N, Singh C, *et al.* Microwave and electrical characterization of M-type Ba_{0.5}Sr_{0.5}Co_xRu_xFe_(12-2x)O₁₉ hexaferrite for practical applications. *Solid State Commun* 2015, **201**: 72–75.
- [16] Singh C, Bindra Narang S, Koledintseva MY. Microwave absorption characteristics of substituted Ba_{0.5}Sr_{0.5}M_xFe_(12-2x)O₁₉ (M = Co²⁺–Zr⁴⁺ and Co²⁺–Ti⁴⁺) sintered ferrite at X-band. *Microw Opt Technol Lett* 2012, **54**: 1661–1665.
- [17] Nikmanesh H, Hoghoghifard S, Hadi-Sichani B. Study of the structural, magnetic, and microwave absorption properties of the simultaneous substitution of several cations in the barium hexaferrite structure. *J Alloys Compd* 2019, **775**: 1101–1108.
- [18] Nikmanesh H, Moradi M, Kameli P, *et al.* Effects of annealing temperature on exchange spring behavior of Barium hexaferrite/nickel zinc ferrite nanocomposites. *J Electron Mater* 2017, **46**: 5933–5941.
- [19] Liu CY, Zhang YJ, Jia JG, *et al.* Multi-susceptible single-phased ceramics with both considerable magnetic and dielectric properties by selectively doping. *Sci Rep* 2015, **5**: 9498.
- [20] Zhivulin VE, Trofimov EA, Zaitseva OV, *et al.* Flux single crystal growth of BaFe_{12-x}Ti_xO₁₉ with titanium gradient. *Crystals* 2020, **10**: 264.
- [21] Gupta S, Upadhyay SK, Siruguri V, *et al.* Observation of magnetoelastic and magnetoelectric coupling in Sc doped BaFe₁₂O₁₉ due to spin-glass-like phase. *J Phys Condens Matter* 2019, **31**: 295701.
- [22] Trukhanov SV, Trukhanov AV, Kostishyn VG, *et al.* Magnetic, dielectric and microwave properties of the BaFe_{12-x}Ga_xO₁₉ (x ≤ 1.2) solid solutions at room temperature. *J Magn Magn Mater* 2017, **442**: 300–310.
- [23] Xu J, Lu QL, Lin JF, *et al.* Enhanced Ferro-/piezoelectric properties of tape-casting-derived Er³⁺-doped Ba_{0.85}Ca_{0.15}Ti_{0.9}Zr_{0.1}O₃ optoelectronic thick films. *J Adv Ceram* 2020, **9**: 693–702.
- [24] Kumar Y, Yadav KL, Shah J, *et al.* Investigation of magnetoelectric effect in lead free K_{0.5}Na_{0.5}NbO₃–BaFe₁₂O₁₉ novel composite system. *J Adv Ceram* 2019, **8**: 333–344.
- [25] Li J, He S, Shi KZ, *et al.* Coexistence of broad-bandwidth and strong microwave absorption in Co²⁺–Zr⁴⁺ co-doped barium ferrite ceramics. *Ceram Int* 2018, **44**: 6953–6958.

- [26] Tsutaoka T, Koga N. Magnetic phase transitions in substituted Barium ferrites $\text{BaFe}_{12-x}(\text{Ti}_{0.5}\text{Co}_{0.5})_x\text{O}_{19}$ ($x = 0-5$). *J Magn Magn Mater* 2013, **325**: 36–41.
- [27] Liu CY, Zhang YJ, Tang Y, *et al.* The tunable magnetic and microwave absorption properties of the $\text{Nb}^{5+}\text{-Ni}^{2+}$ co-doped M-type Barium ferrite. *J Mater Chem C* 2017, **5**: 3461–3472.
- [28] Liu CY, Chen YJ, Yue YY, *et al.* Formation of $\text{BaFe}_{12-x}\text{Nb}_x\text{O}_{19}$ and its high electromagnetic wave absorption properties in millimeter wave frequency range. *J Am Ceram Soc* 2017, **100**: 3999–4010.
- [29] Nikmanesh H, Hoghoghifard S, Hadi-Sichani B, *et al.* Erbium-chromium substituted strontium hexaferrite particles: Characterization of the physical and Ku-band microwave absorption properties. *Mater Sci Eng: B* 2020, **262**: 114796.
- [30] Rodríguez-Carvajal J. Recent advances in magnetic structure determination by neutron powder diffraction. *Phys B: Condens Matter* 1993, **192**: 55–69.
- [31] Wills AS. A new protocol for the determination of magnetic structures using simulated annealing and representational analysis (SARAH). *Phys B: Condens Matter* 2000, **276–278**: 680–681.
- [32] Shao Y, Huang FZ, Xu XY, *et al.* Multi-susceptible single-phase $\text{BaAl}_x\text{Fe}_{12-x}\text{O}_{19}$ ceramics with both improved magnetic and ferroelectric properties. *Appl Phys Lett* 2019, **114**: 242902.
- [33] Watanabe K, Kawabe J. Growth and characterization of minute $\text{BaFe}_{12-2x}\text{Ti}_x\text{Co}_x\text{O}_{19}$ crystals from high-temperature solution. *J Mater Chem* 1997, **7**: 1797–1800.
- [34] Vinnik DA, Zherebtsov DA, Mashkovtseva LS, *et al.* Ti-substituted $\text{BaFe}_{12}\text{O}_{19}$ single crystal growth and characterization. *Cryst Growth Des* 2014, **14**: 5834–5839.
- [35] Gupta T, Chauhan CC, Kagdi AR, *et al.* Investigation on structural, hysteresis, Mössbauer properties and electrical parameters of lightly Erbium substituted X-type $\text{Ba}_2\text{Co}_2\text{Er}_x\text{Fe}_{28-x}\text{O}_{46}$ hexaferrites. *Ceram Int* 2020, **46**: 8209–8226.
- [36] Cheng YK, Ren XH. Permeability and electromagnetic wave absorption properties of sintered Barium hexaferrites with substitution of $\text{Co}^{2+}\text{-Zr}^{4+}$. *J Mater Sci: Mater Electron* 2016, **27**: 772–775.
- [37] Singh C, Narang SB, Hudiara IS, *et al.* Hysteresis analysis of Co–Ti substituted M-type Ba–Sr hexagonal ferrite. *Mater Lett* 2009, **63**: 1921–1924.
- [38] Narang SB, Singh C, Bai Y, *et al.* Microstructure, hysteresis and microwave absorption analysis of $\text{Ba}_{(1-x)}\text{Sr}_x\text{Fe}_{12}\text{O}_{19}$ ferrite. *Mater Chem Phys* 2008, **111**: 225–231.
- [39] Nikmanesh H, Eshraghi M, Karimi S. Cation distribution, magnetic and structural properties of $\text{CoCr}_x\text{Fe}_{2-x}\text{O}_4$: Effect of calcination temperature and chromium substitution. *J Magn Magn Mater* 2019, **471**: 294–303.
- [40] Singh C, Bindra-Narang S, Hudiara IS, *et al.* The effect of Co and Zr substitution on dc magnetic properties of Ba–Sr ferrite. *J Alloys Compd* 2008, **464**: 429–433.
- [41] Alam RS, Moradi M, Nikmanesh H. Influence of multi-walled carbon nanotubes (MWCNTs) volume percentage on the magnetic and microwave absorbing properties of $\text{BaMg}_{0.5}\text{Co}_{0.5}\text{TiFe}_{10}\text{O}_{19}$ /MWCNTs nanocomposites. *Mater Res Bull* 2016, **73**: 261–267.
- [42] Nikmanesh H, Moradi M, Bordbar GH, *et al.* Synthesis of multi-walled carbon nanotube/doped Barium hexaferrite nanocomposites: An investigation of structural, magnetic and microwave absorption properties. *Ceram Int* 2016, **42**: 14342–14349.
- [43] Zhang HW, Rong CB, Du XB, *et al.* Investigation on the coercivity and remanence of single-phase nanocrystalline permanent magnets by micromagnetic finite-element method. *J Magn Magn Mater* 2004, **278**: 127–137.
- [44] Gairola SP, Verma V, Singh A, *et al.* Modified composition of Barium ferrite to act as a microwave absorber in X-band frequencies. *Solid State Commun* 2010, **150**: 147–151.
- [45] Liu JR, Itoh M, Machida KI. Electromagnetic wave absorption properties of $\text{Fe}_{1-x}\text{Co}_x/\text{Y}_2\text{O}_3$ ($x = 0.33, 0.5, 0.67$) nanocomposites in gigahertz range. *J Alloys Compd* 2005, **389**: 265–269.
- [46] Watts CM, Liu XL, Padilla WJ. Metamaterial electromagnetic wave absorbers. *Adv Mater* 2012, **24**: OP98–OP120.
- [47] Liu CY, Xu QK, Tang Y, *et al.* Zr^{4+} doping-controlled permittivity and permeability of $\text{BaFe}_{12-x}\text{Zr}_x\text{O}_{19}$ and the extraordinary EM absorption power in the millimeter wavelength frequency range. *J Mater Chem C* 2016, **4**: 9532–9543.
- [48] Singh J, Singh C, Kaur D, *et al.* Tunable microwave absorption in Co–Al substituted M-type Ba–Sr hexagonal ferrite. *Mater Des* 2016, **110**: 749–761.
- [49] Kaur H, Marwaha A, Singh C, *et al.* Investigation of structural, hysteresis and electromagnetic parameters for microwave absorption application in doped Ba–Sr hexagonal ferrites at X-band. *J Alloys Compd* 2019, **806**: 1220–1229.
- [50] Huo J, Wang L, Yu HJ. Polymeric nanocomposites for electromagnetic wave absorption. *J Mater Sci* 2009, **44**: 3917–3927.

Open Access This article is licensed under a Creative Commons Attribution 4.0 International License, which permits use, sharing, adaptation, distribution and reproduction in any medium or format, as long as you give appropriate credit to the original author(s) and the source, provide a link to the Creative Commons licence, and indicate if changes were made.

The images or other third party material in this article are included in the article's Creative Commons licence, unless indicated otherwise in a credit line to the material. If material is not included in the article's Creative Commons licence and your intended use is not permitted by statutory regulation or exceeds the permitted use, you will need to obtain permission directly from the copyright holder.

To view a copy of this licence, visit <http://creativecommons.org/licenses/by/4.0/>.